The Astrophysical Journal, 952:120 (11pp), 2023 August 1 https://doi.org/10.3847/1538-4357/acd850

A NICER View on the 2020 Magnetar-like Outburst of PSR J1846−0258

Chin-Ping Hu[1], Lucien Kuiper[2], Alice K. Harding[3], George Younes[4,5], Harsha Blumer[6,7], Wynn C. G. Ho[8], Teruaki Enoto[9], Cristóbal M. Espinoza[10,11], and Keith Gendreau[12]
[1] Department of Physics, National Changhua University of Education, Changhua 50007, Taiwan
[2] SRON-Netherlands Institute for Space Research, Niels Bohrweg 4, 2333 CA, Leiden, The Netherlands
[3] Theoretical Division, Los Alamos National Laboratory, Los Alamos, NM 87545, USA; ahardingx@yahoo.com
[4] Department of Physics, The George Washington University, Washington, DC 20052, USA
[5] Astronomy, Physics and Statistics Institute of Sciences (APSIS), The George Washington University, Washington, DC 20052, USA
[6] Department of Physics and Astronomy, West Virginia University, Morgantown, WV 26506, USA
[7] Center for Gravitational Waves and Cosmology, West Virginia University, Chestnut Ridge Research Building, Morgantown, WV 26505, USA
[8] Department of Physics and Astronomy, Haverford College, 370 Lancaster Avenue, Haverford, PA 19041, USA
[9] Extreme Natural Phenomena RIKEN Hakubi Research Team, Cluster for Pioneering Research, RIKEN, 2-1 Hirosawa, Wako, Saitama 351-0198, Japan
[10] Departamento de Física, Universidad de Santiago de Chile (USACH), Av. Victor Jara 3493, Estación Central, Chile
[11] Center for Interdisciplinary Research in Astrophysics and Space Sciences (CIRAS), Universidad de Santiago de Chile, Santiago, Chile
[12] X-Ray Astrophysics Laboratory, NASA Goddard Space Flight Center, Greenbelt, MD 20771, USA
Received 2023 February 23; revised 2023 May 11; accepted 2023 May 22; published 2023 July 21

Abstract

We report on our monitoring of the strong-field magnetar-like pulsar PSR J1846−0258 with the Neutron Star Interior Composition Explorer (NICER) and the timing and spectral evolution during its outburst in 2020 August. Phase-coherent timing solutions were maintained from 2017 March through 2021 November, including a coherent solution throughout the outburst. We detected a large spin-up glitch of magnitude $\Delta\nu/\nu = 3 \times 10^{-6}$ at the start of the outburst and observed an increase in pulsed flux that reached a factor of more than 10 times the quiescent level, a behavior similar to that of the 2006 outburst. Our monitoring observations in 2020 June and July indicate that the flux was rising prior to the Swift announcement of the outburst on 2020 August 1. We also observed several sharp rises in the pulsed flux following the outburst and the flux reached quiescent level by 2020 November. The pulse profile was observed to change shape during the outburst, returning to the preoutburst shape by 2021. Spectral analysis of the pulsed emission of NICER data shows that the flux increases result entirely from a new blackbody component that gradually fades away while the power law remains nearly constant at its quiescent level throughout the outburst. Joint spectral analysis of NICER and simultaneous NuSTAR data confirms this picture. We discuss the interpretation of the magnetar-like outburst and origin of the transient thermal component in the context of both a pulsar-like and a magnetar-like model.

Unified Astronomy Thesaurus concepts: Neutron stars (1108)

1. Introduction

The dividing line between the two neutron star populations, rotation-powered pulsars (RPPs) and magnetars, has been blurring over the past 15 years with the discovery of magnetar-like outbursts from the RPPs PSR J1846−0258 and J1119−6127. Both of these pulsars possess very strong surface dipole magnetic fields that are at the upper end of what is observed for RPPs, with 5×10^{13} G for J1846−0258 and 4×10^{13} G for J1119−6127. The first observed outburst from J1846−0258 occurred in 2006 (Gavriil et al. 2008; Kumar & Safi-Harb 2008), during which the pulsed flux increased by a factor of 5, decaying over several months, and a transient thermal component appeared in addition to the persistent nonthermal emission, whose flux rose by 35% (Kuiper & Hermsen 2009). PSR J1119−6127 experienced a magnetar-like outburst in 2016 (Archibald et al. 2016), but in this case a transient nonthermal power-law component appeared and the quiescent purely thermal pulsed flux increased by a factor of >160. In both outbursts, large spin-up glitches occurred, with $\Delta\nu/\nu = 5.74 \times 10^{-6}$ for J1119−6127 and $\Delta\nu/\nu = 2\text{–}4.4 \times 10^{-6}$ for J1846−0258 (Livingstone et al. 2010).

PSR J1846−0258 was discovered through 0.324 s X-ray pulsations by Gotthelf et al. (2000) and with its high spin-down rate of $\dot{P} = 7 \times 10^{-12}$ s s^{-1} has a characteristic age of $\tau = 723$ yr, making it the youngest known RPP. It is located in the Kes 75 supernova remnant and is surrounded by a compact pulsar wind nebula (Helfand et al. 2003; Ng et al. 2008). Its pulsed emission is still only seen in the X-ray band from 3 to 200 keV with RXTE INTEGRAL (Kuiper & Hermsen 2015) and recently also in soft γ-rays below 100 MeV with Fermi (Kuiper et al. 2018). Its spectral energy distribution (SED) is very similar to that of PSR B1509−58, another young, energetic RPP, with an SED peak around 1–10 MeV and a decline above 30 MeV (Kuiper et al. 2018). However, B1509−58 is a radio pulsar while J1846−0258 is radio quiet. These two pulsars are members of a class of so-called "MeV pulsars" whose SEDs peak at MeV energies, contrary to most other energetic RPPs peaking at GeV energies. The MeV pulsars are a group of 11 rotation-powered pulsars that exhibit strong, nonthermal hard X-ray emission, have broad single pulse profiles, and have no detected gamma-ray pulsations above 1 GeV (Harding & Kalapotharakos 2017; Kuiper et al. 2018). All except one are radio quiet.

In this paper, we will describe our long-term monitoring and timing of J1846−0258 using NICER (and Swift for the pre-2018 era) in Section 2. As a result of this program we have obtained phase-coherent timing solutions from 2017 April

through 2021 November. We will also report on the magnetar-like outburst of 2020 August and its aftermath, during which we obtained target-of-opportunity (ToO) observations following the Swift announcement (Krimm et al. 2020) of a magnetar-like ∼0.1 s flare/burst. Near the start of the outburst we detected a large spin-up glitch (Kuiper et al. 2020) and maintained coherent timing over the entire outburst. Timing through the outburst and the evolution of the pulsed flux and pulse profile are described in Section 3.1. The spectral evolution before and during the outburst are discussed in Section 3.2. Finally in Section 4 we will discuss the implications of these results and how J1846−0258 fits in to the RPP–magnetar connection.

2. Observations and Data Reduction

2.1. NICER Monitoring

We have been timing J1846−0258 with NICER since 2018 May 23 (ObsID 1033290101; MJD 58,261) through a series of Guest Observer proposals, AO1—AO4 GO. The last NICER observation used in this work was performed on 2021 November 13 (ObsID 4607021501; MJD 59,531), and so our NICER monitoring covered a ∼3.5 yr period subjected to ∼3 month (approximately lasting from the end of November until the end of February) regular episodes in which no data can be taken due to visibility constraints resulting in (large) data gaps.

The NICER data were processed using HEASOFT version 6.27.2 and NICERDAS version 7a. We used the latest calibration files obtained from the standard CALDB release for NICER downloaded from NASA's High Energy Astrophysics Science Archive Research Center (HEASARC). We start our data reduction from level 1 event files. We create good time intervals using standard filtering criteria as described in the NICER Data Analysis Guide. For spectral studies, we excluded module numbers 14 and 34 to avoid potential contamination by instrumental noise in the soft energy band.

For the timing analysis, requiring less restrictive selections as for the spectral analysis, we used predominantly the screened event files as stored at HEASARC. Next, we applied a time filter based on the observed count rate in the 12–15 keV band, and we ignored events from periods with high rates in that band. Also events from high-rate modules are ignored. Finally, to search for the pulsed emission from J1846−0258 we used only events with energies in the 2.5–10 keV band, the optimum band. Sometimes the default screening criteria resulted in very small exposure times in which case we used the unfiltered level 1 event files and followed the same screening steps as outlined before.

2.2. NuSTAR Observations

During the 2020 outburst NuSTAR observed J1846−0258 on 2020 August 5 (ObsID 80602315002), 2020 August 20 (ObsID 80602315004), 2020 September 17 (ObsID 80602315006), and 2020 October 09 (ObsID 80602315008). We also used NuSTAR data of J1846−0258 from a ∼95 ks observation taken on 2017 September 17 (ObsID 40301004002) with the source in quiescent state.

The NuSTAR data were reduced using the standard data reduction process with NuSTAR DAS v1.9.2 and CALDB 20191219. We extracted on-source spectra from circular regions of 1′ radius centered at the source position in the 3–70 keV energy band from the NuSTAR observations. For the spectral fitting, we grouped source spectra using the grppha tool of HEASoft, such that each spectral bin would have a minimum of 25 counts.

2.3. Swift Monitoring

In this work we also analyzed data from the X-ray Telescope (XRT; Burrows et al. 2005) on board the Neil Gehrels Swift observatory (Gehrels et al. 2004), operating in Windowed-Timing (WT) mode, providing a time resolution of 1.7675 ms. The Swift-monitoring campaign of J1846−0258 started on 2011 July 25 and ended on 2018 November 19. Data from the early phase of the monitoring program up to and including 2016 September 4 have already been used and analyzed in Kuiper et al. (2018). In order to characterize the spin behavior of J1846−0258 during its quiescent state before the 2020 outburst we analyzed the monitoring data collected between 2016 September 17 and 2018 November 19. More detailed information is given in Section 3.1.1.

3. The 2020 August Outburst

On 2020 August 1, the Swift telescope reported a short-duration (∼0.1 s) flare in the Burst Alert Telescope (BAT) detector from J1846−0258 (Krimm et al. 2020). We started ToO observations on August 2 with NICER, obtaining densely sampled observations of the source until 2020 November 22. From our AO2 GO monitoring observations that started on 2020 March 26, we saw that during the observation performed on 2020 June 26 (MJD 59,026) the pulsed count rate in the 2.5–10 keV band had already increased by a factor of ∼4 with respect to the (preoutburst) quiescent level (Kuiper et al. 2020). The 2020 July 25 (MJD 59,055) observation, performed about a week before the magnetar-like burst, showed an even larger, 10 times higher, 2.5–10 keV pulsed count rate than the preoutburst value. Apparently, the source had already gone into outburst somewhere between 2020 May 27 (MJD 58,996; the last AO2 GO observation of the quiescent period) and 2020 June 26.

Figure 1 shows the 2.5–10 keV pulsed count rate starting from our AO2 observation on 2020 May 27 through the outburst until the count rate reached near quiescent level on 2020 November 22. The Swift/BAT burst announced on 2020 August 1 (Krimm et al. 2020) is marked by the vertical dotted line, which already occurred after the first recorded rate peaked on 2020 July 25. During the ToO observations, we recorded at least three more count-rate peaks with the highest level reached on 2020 August 21. The very dense time sampling reveals that the outburst decay was very nonsteady with possibly many unresolved variations in flux.

Blumer et al. (2021) presented radio observations with the Green Bank Telescope (GBT) and X-ray observations with Chandra of J1846−0258 and its pulsar wind nebula (PWN) following the 2020 outburst. Their GBT observations took place 2020 August 5–6, only a few days after the Swift announcement but actually about 10 days after the initial outburst peak flux. They reported no detectable pulsed radio emission and placed an upper limit of 55 mJy. They also presented results of Chandra ACIS-S observations taken on 2020 September 12, more than one month after the outburst. Fitting the total (=pulsed plus unpulsed) X-ray spectrum with a power law plus blackbody, they reported a softer power-law index of $\Gamma = 1.7 \pm 0.3$ compared to the quiescent value of

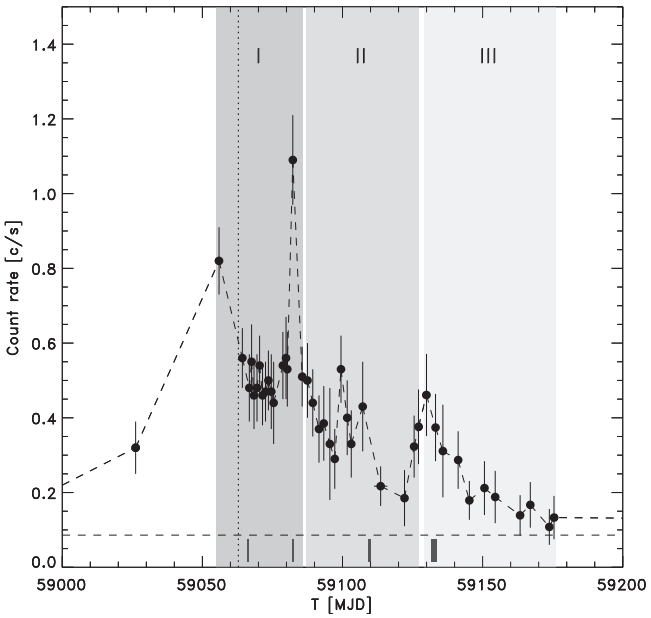

Figure 1. Pulsed count rate (2.510 keV) of J1846−0258 from NICER data taken between 2020 June 26 and 2020 November 22. The vertical dotted line indicates the date of the magnetar-like ∼0.1 s burst detected by Swift. The horizontal long-dashed line is the quiescent count-rate level. The gray areas—indicated by the numbers I, II, and III—covering the 2020 outburst era specify the three data periods for which we have phase-coherent timing solutions (see Table 1, entries 5–7). The four black bars at the bottom of the plot refer to the four NuSTAR observations performed during the full outburst period.

$\Gamma = 1.2 \pm 0.1$ and the appearance of a thermal component with temperature $kT = 0.7 \pm 0.1$ keV. Their measured 0.5–10 keV flux was 2.4 times the quiescent flux level, consistent with our NICER count rate on that date (see Figure 1). They detected no significant increase in X-ray flux or spectral index of the PWN. Livingstone et al. (2011) also found no change in X-ray flux or spectrum of the PWN following the 2006 outburst.

3.1. Timing Analysis

In this work, constituting an extension of the timing analyses presented in earlier work by Kuiper & Hermsen (2009) and Kuiper et al. (2018), we performed timing analyses of the preoutburst, outburst, and postoutburst episodes of the 2020 outburst using data from NICER and (for a part of the preoutburst period, 2017–2018) Swift-monitoring observations to make comparisons between quiescent and outburst states possible. Swift and NICER monitoring overlapped between 2018 May–November enabling cross-checking and verification of the timing characteristics.

These analyses yielded phase-coherent timing models (ephemerides) in terms of three, sometimes four, timing parameters specifying the frequency ν, frequency derivative $\dot{\nu}$, and frequency second-order $\ddot{\nu}$ and third-order $\dddot{\nu}$ derivatives evaluated at a certain epoch t_0. These models accurately describe the rotation behavior of the pulsar as a function of time, and so track the spin evolution of the source.

Pulse-phase-folding timing data from any instrument using these ephemerides, adopting different energy selections, yielded energy-resolved pulse-phase distributions, often called pulse profiles. From these the pulse shape as a function of energy can be determined for any emission state of the pulsar.

The models also enable us to separate at any epoch the pulsed emission component from the total emission that has contributions from the surrounding PWN and supernova remnant, and the pulsar itself either pulsed or unpulsed. So we can study the pulsed flux (or count rate) as a function of time, probing the outburst.

3.1.1. Timing Models (Ephemerides)

The first step in the timing analysis is the conversion of spacecraft arrival times (usually evaluated in TT or TDT time system) to solar system barycentered times (TDB time frame) using the instantaneous spacecraft ephemeris (specifying the position and velocity of the spacecraft), solar system ephemeris (in this work JPL-DE200), a Chandra X-ray based accurate location of the pulsar (Helfand et al. 2003), and for Swift up-to-date clock-correction information. We performed this barycentering process for Swift/XRT (WT-mode) observations 00032031149—00032031216 executed between 2016 September 15 and 2018 November 19 (MJD 57,646—58,441). An equivalent (IDL-based) barycentering procedure was used for the NICER observations.

From the barycentered Swift and NICER event lists of each observation (or combination of observations if the exposure of a single observation was too low) we derived so-called pulse arrival times (ToAs). For Swift/XRT (2.5–10 keV) on average we typically needed 15–20 ks net exposure time to detect the timing signal of J1846−0258 above 3σ in a 25″ extraction area centered on the source (see, e.g., Section 3.1.2 of Kuiper et al. 2018). For NICER (2.5–10 keV) the required net exposure is typically 5–8 ks to reach a significant pulsed signal detection depending on the instantaneous background rate.

From these ToAs we constructed phase-coherent timing models covering a ∼4.5 year period from 2017 April 28 until 2021 November 14 according to the method outlined in Section 4 of Kuiper & Hermsen (2009). The results are listed in Table 1 and consist of eight separate models: four covering the preoutburst episode (entries 1–4, of which 1–2 are solely based on Swift monitoring), three covering the (densely sampled) outburst period (entries 5–7), and finally two covering the postoutburst era (entries 8–9). The spin evolution of J1846−0258 since its discovery in 1999 April with respect to the pre-2006 outburst ephemeris is shown in the left panel of Figure 2, while the right panel zooms in on the time period analyzed in this work. In the latter period from early-2016 September until mid-2021 November we discovered several timing discontinuities in both ν and $\dot{\nu}$, which are summarized below:

1. MJD 57,635–57,871 (2016 September 4–2017 April 28): A clear glitch in $\dot{\nu}$ showing an acceleration in the spin-down rate occurring just before or in the 2016–2017 Swift-monitoring data gap.
2. MJD 58,061–58,167 (2017 November 4–2018 February 18): Phase-coherence loss during the 2017–2018 Swift-monitoring data gap.
3. MJD 58,671–58,698 (2019 July 7–2019 August 3): A small glitch of fractional size $\Delta\nu_g/\nu_g = (7.3 \pm 0.4) \times 10^{-8}$ occurred during the NICER monitoring. In spite of its small amplitude, the glitch could be well characterized because of the densely sampled NICER ToO observations in the postglitch period. Changes in both $\dot{\nu}$ and $\ddot{\nu}$ were also detected, with values $\Delta\dot{\nu}_g/\dot{\nu}_g = (4.5 \pm 0.3) \times 10^{-4}$ and $\Delta\ddot{\nu}_g = (2.66 \pm 0.13) \times 10^{-21}$ Hz s^{-2}, all evaluated at an assumed glitch epoch t_g of MJD 58,685. This timing glitch could easily be distinguished from red noise.

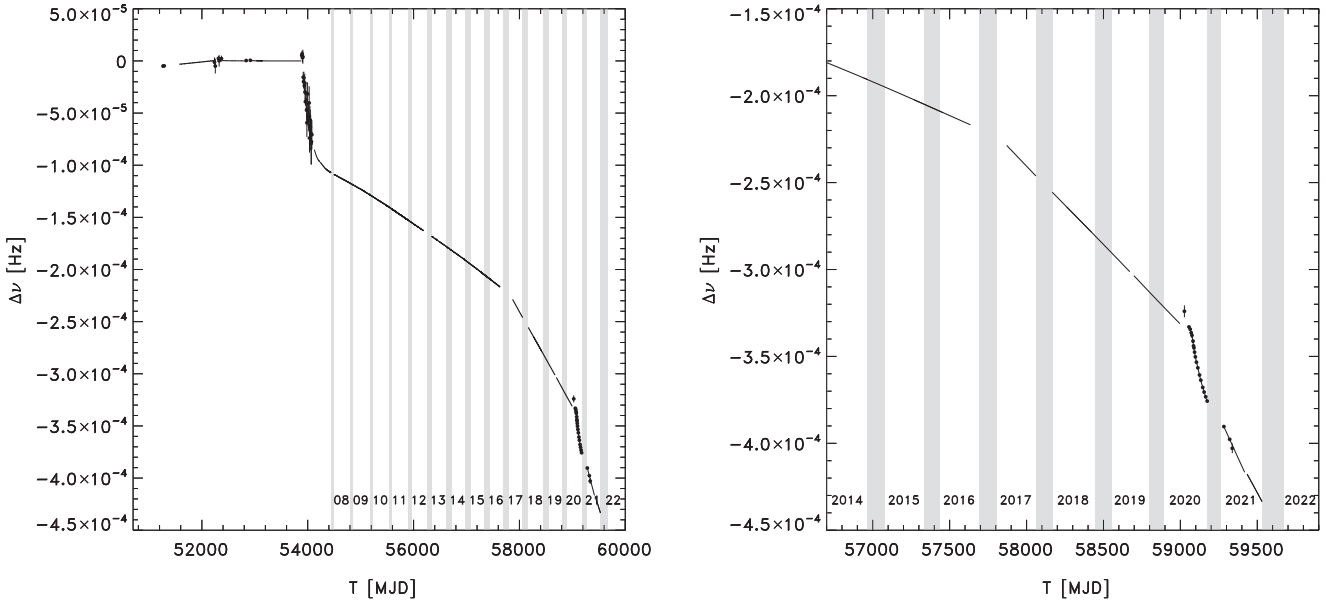

Figure 2. Left: spin frequency evolution $\Delta\nu(t)$ of J1846−0258 (relative to the pre-2006 outburst ephemeris; see, e.g., Gavriil et al. 2008; Livingstone et al. 2010, 2011; Kuiper & Hermsen 2015) since its discovery in RXTE-PCA data from 1999 April up to 2021 November. The 2006 and 2020 glitches are clearly visible near MJD 54,000 and MJD 59,000, as well as an (accelerated) spin-down rate feature/glitch that pops up around MJD 57,700 near/during the Swift 2016–2017 observation gap. Right: zoom in of the rotation frequency evolution during the period of Swift/XRT and NICER timing from early 2014 until 2021 November. Swift and NICER data gaps are shown as gray hatched vertical areas.

Table 1
Phase-coherent Ephemerides for PSR J1846−0258 as Derived from NICER/XTI and Swift/XRT (Monitoring) Data Covering the Time Period MJD 57,871–59,532 (2017 April 28—2021 November 14)

Entry[a] No.	Start (MJD)	End (MJD)	t_0, Epoch (MJD,TDB)	ν (Hz)	$\dot{\nu}$ (10^{-11} Hz s^{-1})	$\ddot{\nu}$ (10^{-21} Hz s^{-2})	$\dddot{\nu}$ (10^{-24} Hz s^{-3})	rms[b]	Φ_0[c]
				Preoutburst 2020					
1	57,871	58,061	57,956.0	3.044 250 906(4)	−6.636 32(7)	4.63(79)	0.0	0.044	0.4167
2	58,167	58,422	58,402.0	3.041 697 558(20)	−6.619 07(50)	3.67(54)	0.0	0.025	0.4258
3	58,261	58,671	58,312.0	3.042 212 358(3)	−6.621 40(4)	2.93(3)	0.0	0.029	0.1074
4	58,698	58,996	58,893.0	3.038 892 369(2)	−6.604 60(3)	5.72(9)	0.0	0.042	0.9539
				Outburst 2020					
5	59,055	59,086	59,064.0	3.037 919 719(23)	−6.725 6(25)	−2659(45)	0.0	0.038	0.8216
6	59,087	59,129	59,099.0	3.037 707 087(50)	−7.018 0(52)	1776(98)	−1.37(14)	0.026	0.1456
7	59,129	59,175	59,145.0	3.037 432 343(15)	−6.849 8(12)	298(22)	0.0	0.038	0.4163
				Postoutburst 2020					
8	59,281	59,418	59,318.0	3.036 433 103(8)	−6.709 6(2)	5.6(1.0)	0.0	0.022	0.0535
9	59,434	59,532	59,523.0	3.035 250 253(16)	−6.667 2(4)	0.0	0.0	0.018	0.7372

Notes. Entries 1–2 are solely Swift/XRT ToA based covering 2017 April 28–November 4 (entry 1) and 2018 February 18–November 19 (entry 2), entry 3 is based on a combination of Swift/XRT and NICER ToAs starting at the first NICER observation performed on 2018 May 23 (MJD 58,261), and entries 4–9 are solely NICER TOA based.

[a] Solar system planetary ephemeris DE200 has been used in the barycentering process.

[b] The rms is the root-mean-square of the deviation from the best fit in phase units.

[c] Φ_0 is the phase offset to apply in the phase calculation to obtain consistent alignment (see, e.g., Equation (1) in Kuiper et al. 2018).

4. MJD 58,996–59,055 (2020 May 27–2020 July 25): A strong glitch of fractional size $\Delta\nu_g/\nu_g \sim 3 \times 10^{-6}$, comparable in size to the 2006 outburst (see Section 4.2 of Kuiper & Hermsen 2009 for more details), heralded very likely the start of the 2020 outburst of J1846−0258.
5. MJD 59,175–59,281 (November 11, 2020–2021 March 8): Phase-coherence loss during the NICER 2020–2021 data gap of ∼3.4 month duration due to one or more glitches.
6. MJD 59,418–59,434 (2021 July 23–2021 August 8): A small glitch of fractional size $\Delta\nu_g/\nu_g \sim (0.5 - 0.66) \times 10^{-6}$ occurred during regular monthly NICER monitoring.

A linear fit to the spin-down rates in Table 1 gives an indication of the effective evolution of this quantity on time, with $\ddot{\nu} = 3.9(3) \times 10^{-21}$ Hz s^{-2}. This indicates a braking index before the outburst (Swift + NICER data) of $n = 2.7 \pm 0.2$. Interestingly, the braking index after the 2006 outburst was seen to decrease from 2.65 ± 0.01 to 2.16 ± 0.13

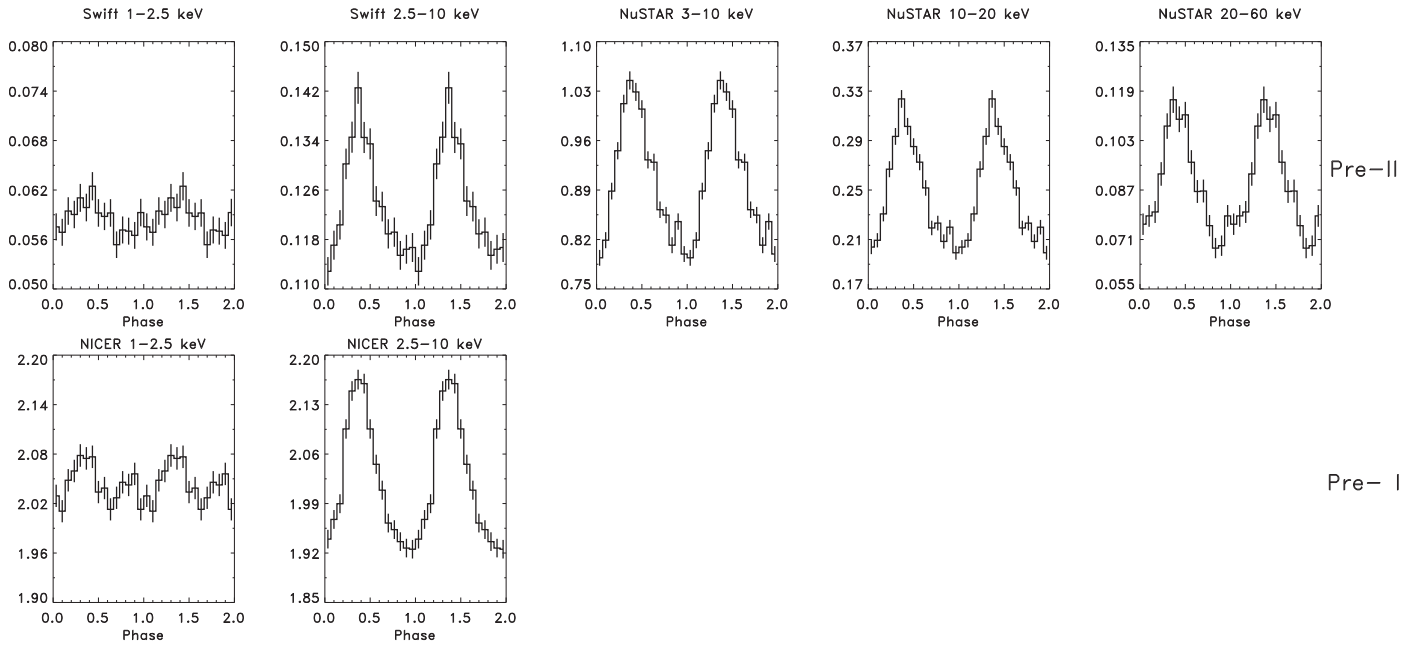

Figure 3. Pulse profiles of J1846−0258 for different stages prior to the 2020 outburst, indicated by Pre-II (Swift 2017–2018; MJD 57,871–58,442; 2017 April 28–2018 November 20 totaling an exposure time of 319.4 ks, NuSTAR 2017 September 17–20; exposure time ∼95 ks) and Pre-I (NICER 2018—2020 preoutburst; MJD 58,261–58,996; 2018 May 23–2020 May 27; exposure time ∼166.7 ks), for different energy bands as observed by Swift, NICER, and NuSTAR. Along the *y*-axis the count rate (in cts s^{-1}) is shown. Error bars are at 1σ confidence.

(Livingstone et al. 2011). Our preliminary measurement indicates that between 2006 and 2020 the rotation somehow went back to its original pre-2006 outburst evolution. There is still not enough data to measure the braking index after the 2020 outburst.

3.1.2. Pulse Profile Evolution

We applied the timing models listed in Table 1 in a pulse-phase folding procedure to obtain pulse-phase distributions for several different energy bands for the preoutburst period (split into two parts related to Swift and NICER monitoring), for the outburst episode subdivided into three parts driven by ephemeris validity constraints, and finally for the postoutburst era. The resulting phase distributions are shown in Figures 3, 4, and 5 for the preoutburst, outburst, and postoutburst periods, respectively.

The preoutburst period running from 2017 April 28 to 2020 May 27 was subdivided into two parts with Swift (Pre-II; MJD 57,871–58,442) and NICER (Pre-I; MJD 58,261–58,996) monitoring. Pulse-phase folding 51 Swift observations, totaling 319.402 ks exposure time, resulted in the phase distributions shown in the upper left two frames of Figure 3 with Z_2^2 significances of 2.8σ and 13.0σ for the 1–2.5 and 2.5–10 keV bands, respectively. During the Swift-monitoring period NuSTAR also observed J1846−0258 during 2017 September 17–20 for ∼95 ks while the source was in quiescent state. The well-known pulse shape (see, e.g., Figure 3 of Kuiper & Hermsen 2009) is clearly visible up to ∼60 keV in these NuSTAR data (see the upper right three panels of Figure 3). The second part of the preoutburst period (Pre-I) referred to solely NICER monitoring observations comprising 166.67 ks of (screened) exposure time. The corresponding pulse-phase distributions are shown in the lower left panels of Figure 3 for the 1–2.5 (Z_2^2 significance of 4.8σ) and 2.5–10 keV bands.

The postoutburst period from 2021 March 8 to November 13 (MJD 59,281–59,531) using merely NICER monitoring observations, totaling 103.55 ks of screened exposure time, shows pulse-phase distributions for the 1–2.5 (Z_2^2 significance of 4.1σ) and 2.5–10 keV bands (see Figure 5) equivalent in shape and strength to the corresponding NICER preoutburst distributions.

It is clear from the pre- and postoutburst observations, representing the quiescent state, that the pulsed emission in the 1–2.5 keV band is weak, mainly coming from events with measured energies in the range 2–2.5 keV.

The situation changed dramatically during the outburst episode (2020 July 25–November 22; MJD 59,055–59,175) that was split into three smaller time segments, indicated by I, II, and III (NICER screened exposures 86.014, 40.694, and 20.064 ks, respectively), driven by phase coherency[13] (see Table 1).

Figure 4 shows the evolution of the pulse morphology and strength for different energy bands during different stages of the outburst as observed by NICER and NuSTAR. The leftmost column showing the NICER 1–2.5 keV lightcurves demonstrates the emergence of a very strong (soft) pulsed emission component that gradually fades away toward its quiescent level. The pulsed significance Z_2^2 in the 1–2.5 keV band evolves from 31.5σ to 15.2σ to 6.0σ for the three segments I, II, and III, respectively.

Both the NICER 2.5–10 keV and NuSTAR 3–10 keV bands show a similar fading evolution; however, contrary to the quiescent pulse morphology a prominent "shoulder" or bump appears during segment I observations near phase ∼0.2 before primary maximum at phase 0.37. This feature also fades away in course of the outburst. It is also clear from the 1–2.5, 2.5–10,

[13] During a regular NICER monitoring observation on 2020 June 26 (MJD 59,026) the source was already in outburst; however, we could not phase connect its timing data.

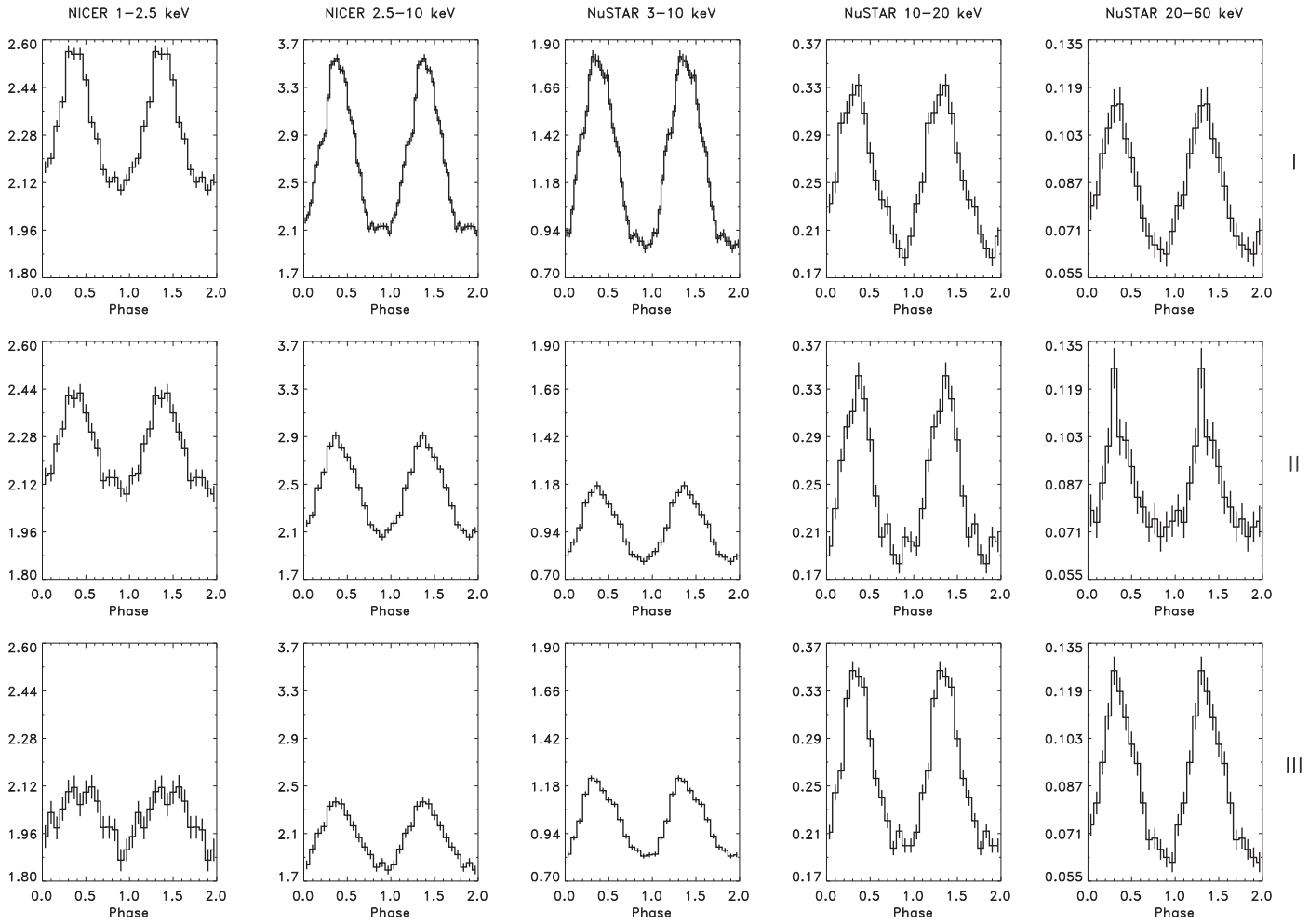

Figure 4. Pulse profiles of J1846−0258 during different phases of the 2020 outburst, indicated by I (MJD 59,055–59,086; 2020 July 25–August 24), II (MJD 59,087–59,127; 2020 August 26–October 5), and III (MJD 59,129–59,175; 2020 October 7–November 22, for different energy bands as observed by NICER and NuSTAR. NuSTAR observed J1846−0258 on 2020 August 5 and August 20, during segment I, on 2020 September 17 during II, and 2020 October 9 during III. Along the *y*-axis the count rate (in cts s^{-1}) is shown. Error bars are at 1σ confidence. The columns show the pulse profiles for a certain energy band for either NICER or NuSTAR with a fixed range in ordinate making comparisons between profiles from different outburst phases more comfortable. Significant changes in shape of the pulse-phase distributions and intensity of the pulsed emission are only detectable below $\lesssim$10 keV.

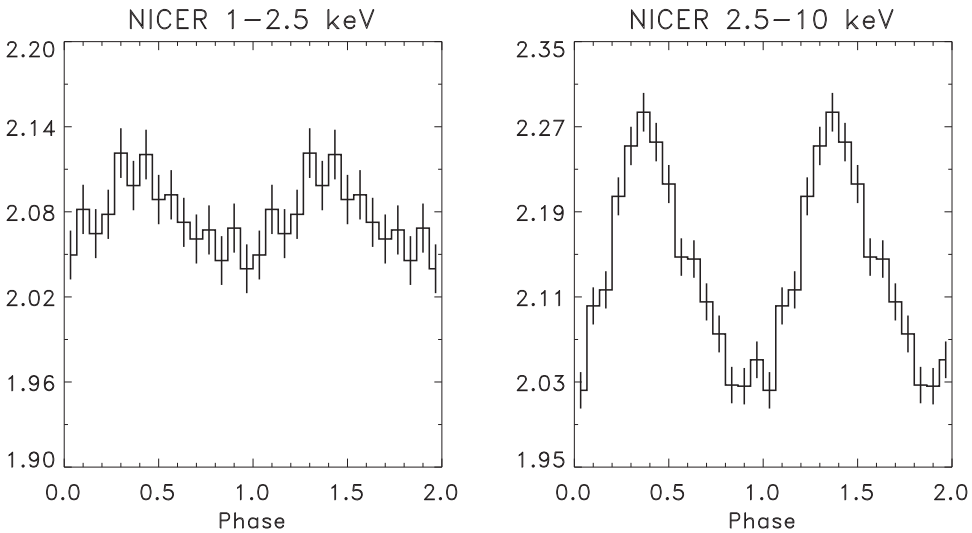

Figure 5. Pulse profiles of J1846−0258 for the postoutburst 2020 period (MJD 59,281–59,531; 2021 March 8–November 13) as observed by NICER in two different energy bands. Along the *y*-axis the count rate (in cts s^{-1}) is shown. Error bars are at 1σ.

Table 2
Best-fit Parameters of Joint NuSTAR–NICER Observations

Time (MJD)	NuSTAR ObsID	NICER ObsID	Γ	$kT_{\rm BB}$ (keV)	$R_{\rm BB}$ (km)
59,066	80602315002	3033290103	$1.4^{+0.5}_{-0.3}$	0.93 ± 0.08	0.6 ± 0.3
59,081	80602315004	3033290115,116	$1.3^{+0.3}_{-0.5}$	$1.01^{+0.06}_{-0.05}$	$0.9^{+0.3}_{-0.2}$
59,109	80602315006	3033290126,127	1.4 ± 0.2	$0.5^{+0.2}_{-0.1}$	4^{+14}_{-3}
59,131	80602315008	3033290132,135,136	1.1 ± 0.1	0.8 ± 0.1	$0.6^{+1.2}_{-0.3}$

and 3–10 keV pulse-phase distributions that an underlying enhanced DC (unpulsed) component appeared that fades away across the outburst.

On the contrary, the pulsed emission above 10 keV as shown by NuSTAR in the two rightmost columns of Figure 4 seems to not vary dramatically and is comparable to its quiescent-state properties (see Figure 3, Pre-II—right two panels).

3.1.3. Pulsed Flux Evolution during the 2020 Outburst

From the pulse-phase distributions per observation (or combination of observations) pulsed excess counts can be determined for any energy band by estimating the excess counts above the DC or unpulsed level evaluated from the 0.8–1.05 phase window (off-pulse phase; see, e.g., Figure 3 of Kuiper & Hermsen 2009). These pulsed excess counts are subsequently converted to rates using the (screened) exposure times of the involved observation(s). The 2.5–10 keV pulsed count rate across the 2020 outburst episode as observed by NICER is shown in Figure 1. The different segments—I, II, and III—are hatched, while solid vertical bars at the bottom of the plot indicate the performed NuSTAR observations. The horizontal dashed line represents the quiescent 2.5–10 keV level, and the vertical dotted line indicates the Swift detection of the magnetar-like $\sim$0.1 s burst (Krimm et al. 2020), triggering our NICER ToO program. It is clear from this plot that J1846−0258 was already in outburst before the occurrence of the magnetar-like burst. Several reflarings are also visible in Figure 1, in particular the one on 2020 August 21 (MJD 59,082). Initially, we suspected that this was a statistical fluke; however, a deeper study reveals that this enhancement of about 1 hr duration was also clearly detectable in a contemporaneous NuSTAR observation (ObsID 80602315004), and so demonstrates the validity of the event. The feature mimics a mini-outburst, for the first time introduced by Kuiper et al. (2012, see their Section 3.1.1) in the study of the high-energy characteristics of the 2008 and 2009 outbursts of magnetar 1E1547.0−5408.

The quiescent-state level is reached near MJD 59,175 (2020 November 22), the last NICER observation before the 2020–2021 data gap.

3.2. Spectral Evolution

We carried out spectral fits on the pulsed component only, meaning that the photons collected during off-pulse phases were treated as background and subtracted from the on-pulse spectra. To examine the broadband spectral behavior of the pulsed emission, we first jointly fit NICER and NuSTAR spectra at four different epochs. We used the tbabs model with corresponding interstellar medium abundance as described in Wilms et al. (2000) to determine the hydrogen column density ($N_{\rm H}$) and linked this parameter across all data sets. The spectra were fit with a two-component model consisting of a hard power law and a soft blackbody. The parameters of these two components are linked between data sets obtained at the same epoch. An additional constant component was introduced to account for the cross-calibration between instruments and the flux difference between data sets.

The first NuSTAR observation (ObsID 80602315002) was made together with NICER ObsID 3033290103 on MJD 59,066, and we fit these two data sets by linking all the spectral parameters. The other three NuSTAR observations did not have corresponding NICER observations on the same dates, so we performed simultaneous fits with nearby NICER observations that bracketed the NuSTAR ones. For example, we jointly fit the NuSTAR observation on MJD 59,081 (ObsID 80602315004) with NICER observations on MJD 59,080 and 59,082. Similar work was done for observations on MJD 59,109 (ObsID 80602315006) and MJD 59,131 (ObsID 80602315008). The results are shown in Table 2, and the unfolded spectra of these four data sets are shown in Figure 6. The $N_{\rm H}$ was constrained to be $(6.1 \pm 0.8) \times 10^{22}$ cm^{-2}. The photon indices of these four data sets varied slightly but remained consistent at around $\Gamma \approx 1.2$. On the other hand, the blackbody component varied significantly, indicating that the flux variability during the outburst is dominated by changes in the blackbody component. This can also be seen from the pulse profiles as a function of energy.

We then traced the spectral evolution in the soft X-ray band using all NICER data sets. We tried to fit individual data sets by freezing the $N_{\rm H}$ at 6.1×10^{22} cm^{-2} and allowing all the blackbody and power-law parameters to be free. However, the NICER energy range is not sensitive to the hard power-law component, and the spectral parameters could not be well constrained. Therefore, we froze the Γ at 1.2 and allowed the $kT_{\rm BB}$, $R_{\rm BB}$, and power-law normalization to be free parameters in the following analysis. Additionally, the number of X-ray photons decreased as the flux decreased and the exposure time of each observation was different. Therefore, we jointly fit one to three data sets by linking the aforementioned three spectral parameters. The resulting unabsorbed fluxes in the 1–10 keV band, fluxes of individual components in the same energy band, and three spectral parameters are shown in Figure 7, and the parameters are shown in Table 3. The overall flux, $kT_{\rm BB}$, and blackbody flux decreased over time. A mini-flare on MJD 59,082 (August 21) is observed. During the flare, the $kT_{\rm BB}$ and flux increased. On the other hand, the power-law flux remained constant throughout the entire observation run, suggesting that the outburst is dominated by the increase of the surface emission. A few days after the flare, the blackbody component could not be well constrained and the power law dominated the spectrum in the soft X-ray band.

4. Discussion

The 2020 August X-ray outburst was the second magnetar-like outburst from PSR J1846−0258 since its discovery in

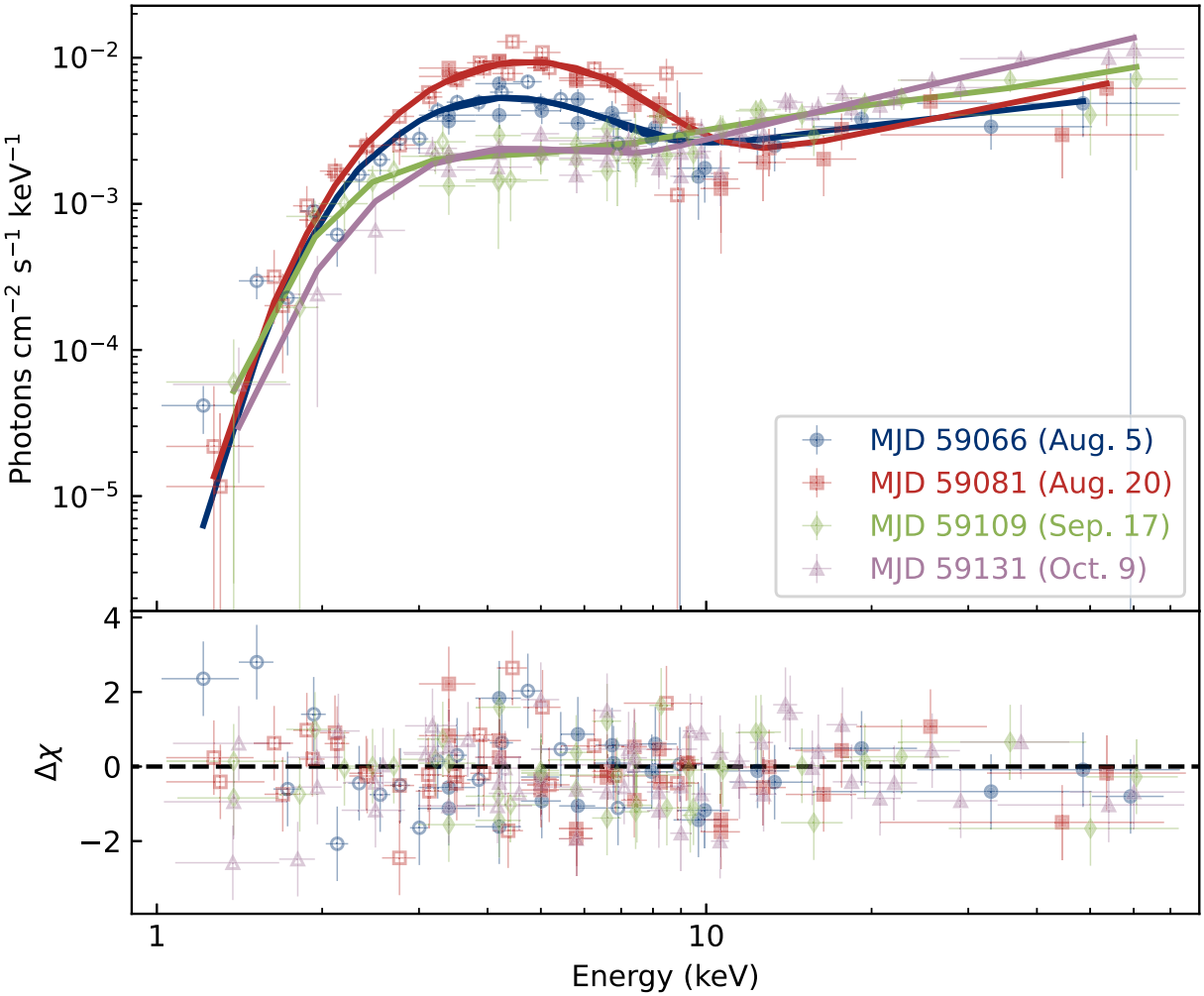

Figure 6. Spectra extracted from NICER data (open points) and NuSTAR data (closed points). The solid lines indicate the best-fitting model to data with the corresponding color. The bottom panel shows the corresponding residuals in terms of σ.

1999, after a 14 yr hiatus since its first recorded outburst in 2006. Our NICER GO and ToO observations provided continuous monitoring and timing of the source starting about 3.5 yr before the 2020 outburst until more than 1 yr following the outburst in 2021 November. Our monitoring observations prior to the 2020 August 1 Swift announcement of the outburst showed that the flux was already increasing above quiescent level by late June. Due to our high-cadence observations during and following the outburst, we were able to resolve rapid changes in the pulsed flux, which our measurements showed increased by more than a factor of 10 above the quiescent level. While this flux increase is much higher than the 5 times increase reported for the 2006 outburst (Kuiper & Hermsen 2009), the flux during that outburst was less densely sampled and timing coherence was lost (Gavriil et al. 2008), so higher flux peaks may have been missed. Both outbursts were accompanied by spin-up glitches of very similar size and in both cases, transient thermal components appeared that were responsible for most of the flux increases. The thermal components and the flux also decayed over similar timescales of several months. However, we observed a change in the X-ray pulse profile during the 2020 outburst, while no change in profile was reported for the 2006 outburst. Overall, the characteristics of the two magnetar-like outbursts of J1846−0258 are very similar.

PSR J1846−0258 thus appears to be a unique and fascinating source with a dual nature, behaving most of the time like an RPP and occasionally like a magnetar. It is also an unusual young RPP, having no detected radio or GeV emission. So is it an RPP that is becoming a magnetar, or a magnetar masquerading as an RPP? As we discuss below, the quiescent behavior as well as the outbursts can be interpreted in either scenario but involve very different physical mechanisms for the emission.

First, we consider a pulsar-like model for PSR J1846−0258. Harding & Kalapotharakos (2017) presented a model for MeV pulsars like J1846−0258 in which their lack of radio or GeV emission is due to geometry. In this model, MeV pulsars are the same as the rest of the young RPP population: they have global dipole magnetospheres that are nearly force-free, emit radio emission from above the magnetic poles and γ-ray and nonthermal X-ray emission from near the current sheet outside the light cylinder (Kalapotharakos et al. 2018; Harding et al. 2021). However, they have small magnetic inclination angles and we view them along lines-of-sight, away from the magnetic poles, that miss both the radio beams and the center of the current sheet where the highest-energy acceleration occurs and where the GeV emission is produced. In this model then, the quiescent X-ray emission is synchrotron radiation (SR) from electron–positron pairs near the current sheet, where the shape

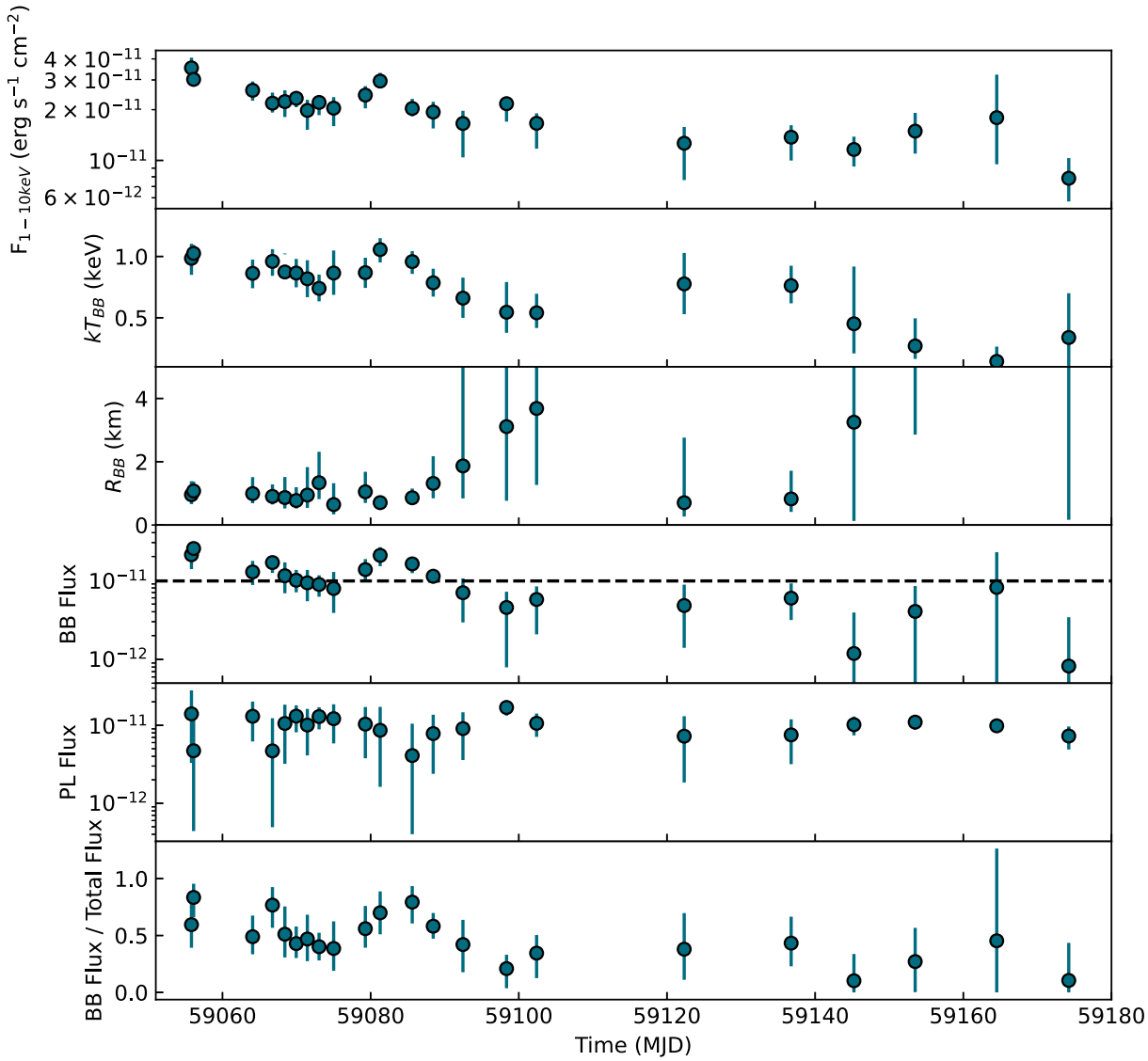

Figure 7. Spectral evolution of the pulsed emission of J1846−0258 observed with NICER following the outburst on 2020 August 1. From top to bottom, panels show the evolution of the unabsorbed flux in the 1–10 keV band (in units of erg cm^{-2} s^{-1}), the blackbody temperature (in units of keV), the emitting radius (assuming a distance of 6.5 kpc), the BB flux, PL flux, and the ratio of BB flux to the total flux. The horizontal dashed line denotes the mean value of the PL flux across all data sets.

of the SED derives from the smoothly falling spectrum of the pairs (Harding & Kalapotharakos 2015; Harding et al. 2021). The magnetar-like outbursts of J1846−0258 are due to the appearance of or a change in a toroidal surface magnetic field component that provides a field twist, and more particle acceleration and pair production near the surface. The increased pair multiplicity increases the polar cap heating and opens up more field lines, increasing the size of the polar caps. If our line of sight then crosses nearer to the larger heated polar cap, we will temporarily see a thermal component, but we can still miss the radio emission since it is more tightly beamed than the thermal emission. However, in this case the thermal component will not be in phase with the nonthermal SR pulse, which is a major drawback for this model. The measurements of a braking index in J1846−0258 (Livingstone et al. 2011) with values typical of RPPs may add support to the RPP model. However, it is unclear what we should expect for magnetar braking indices and why they have not been detected.

Next, we consider a magnetar-like model in which the quiescent X-ray emission from J1846−0258 is resonant inverse-Compton scattering emission (RICS) from particles accelerated by field twists and scattering thermal photons from the hot neutron star surface (Baring & Harding 2007; Beloborodov 2013). We do not see any GeV emission because photon splitting and pair production attenuate the RICS spectrum above about 1 MeV (Wadiasingh et al. 2019). The outbursts are then typical magnetar bursts where crustal motions cause increases in the magnetic field twists, particle acceleration, and RICS emission. The increased particle acceleration and pair/splitting cascades produce visible heated spots due to particle surface bombardment (Beloborodov 2013). Since this emission occurs on closed field lines near the equator, we could miss any transient radio emission along open field lines. There are several potential drawbacks in this model. If the quiescent emission is RICS, why do we not see a quiescent thermal component as appears in magnetars? Supporting the nonobserved thermal component, many/most young magnetars have X-ray

Table 3
Best-fit Parameters of NICER Observations

Time (MJD)	NICER ObsID	kT_{BB} (keV)	R_{BB} (km)	Flux (10^{-11} erg s^{-1} cm^{-2})	BB Flux (10^{-11} erg s^{-1} cm^{-2})
59,056	3598010801	1.0 ± 0.1	$1.0^{+0.4}_{-0.3}$	$3.5^{+0.5}_{-0.4}$	$2.1^{+0.8}_{-0.7}$
59,056	3598010802	$1.03^{+0.07}_{-0.09}$	$1.1^{+0.3}_{-0.2}$	$3.0^{+0.4}_{-0.3}$	$2.5^{+0.4}_{-0.5}$
59,064	3033290101,102	0.9 ± 0.1	$1.0^{+0.5}_{-0.3}$	2.6 ± 0.3	$1.3^{+0.5}_{-0.4}$
59,067	3033290103	1.0 ± 0.1	$0.9^{+0.4}_{-0.3}$	2.2 ± 0.3	$1.7^{+0.3}_{-0.4}$
59,068	3033290105	0.9 ± 0.1	$0.9^{+0.6}_{-0.3}$	2.2 ± 0.4	1.1 ± 0.5
59,070	3033290106,107	0.9 ± 0.1	$0.8^{+0.4}_{-0.3}$	$2.3^{+0.2}_{-0.3}$	$1.0^{+0.4}_{-0.3}$
59,072	3033290108	0.8 ± 0.2	$0.9^{+0.9}_{-0.4}$	$2.0^{+0.3}_{-0.5}$	0.9 ± 0.4
59,073	3033290109,110	0.7 ± 0.1	$1.3^{+0.9}_{-0.5}$	$2.2^{+0.2}_{-0.4}$	0.9 ± 0.3
59,075	3033290111,112	0.9 ± 0.2	$0.6^{+0.7}_{-0.3}$	$2.0^{+0.3}_{-0.4}$	$0.8^{+0.5}_{-0.4}$
59,079	3033290113,114	0.9 ± 0.1	$1.1^{+0.6}_{-0.3}$	$2.4^{+0.3}_{-0.4}$	$1.4^{+0.5}_{-0.4}$
59,081	3033290115,116	$1.06^{+0.09}_{-0.11}$	0.7 ± 0.2	$3.0^{+0.4}_{-0.3}$	2.1 ± 0.6
59,086	3598010901	$0.96^{+0.08}_{-0.10}$	$0.8^{+0.3}_{-0.2}$	$2.0^{+0.3}_{-0.2}$	$1.6^{+0.3}_{-0.4}$
59,088	3033290117,118	0.8 ± 0.1	$1.3^{+0.9}_{-0.5}$	$1.9^{+0.3}_{-0.4}$	1.1 ± 0.2
59,092	3033290119,120	0.7 ± 0.2	2^{+4}_{-1}	$1.7^{+0.3}_{-0.6}$	0.7 ± 0.4
59,098	3033290122,123	0.5 ± 0.2	3^{+14}_{-2}	$2.2^{+0.2}_{-0.5}$	$0.5^{+0.3}_{-0.4}$
59,102	3033290124,125,126	$0.5^{+0.2}_{-0.1}$	4^{+9}_{-2}	$1.7^{+0.2}_{-0.5}$	$0.6^{+0.3}_{-0.4}$
59,122	3033290128,131,132	$0.8^{+0.3}_{-0.2}$	$0.7^{+2.0}_{-0.4}$	$1.3^{+0.3}_{-0.5}$	$0.5^{+0.4}_{-0.3}$
59,137	3033290135,136,137	$0.8^{+0.2}_{-0.1}$	$0.8^{+0.9}_{-0.4}$	$1.4^{+0.3}_{-0.4}$	0.6 ± 0.3
59,145	3598011101	$0.5^{+0.5}_{-0.2}$	<28	1.2 ± 0.2	<0.4
59,154	3033290139,141,143	$0.3^{+0.2}_{-0.1}$	<6000	1.5 ± 0.4	<0.8
59,165	3033290114,146,147	$0.14^{+0.12}_{-0.04}$	$<1 \times 10^8$	$1.8^{+1.4}_{-0.8}$	<2.2
59,174	3033290150,3598011201,202	$0.3^{+0.4}_{-0.2}$	$<3 \times 10^7$	0.8 ± 0.2	<1.1

Note. The fluxes are calculated in the energy range of 1–10 keV.

luminosities 10^{34}–10^{35} erg s^{-1} (see, e.g., magnetar review by Kaspi & Beloborodov 2017), which would translate to fluxes $\sim 2 \times 10^{-12}$–10^{-11} erg s^{-1} cm^{-2} at 6.5 kpc, lower than the observed fluxes in Table 3. Perhaps this component is much weaker or nonexistent for J1846−0258 because its magnetic activity is not persistent enough to produce heated spots from particle bombardment, and with the geometry for J1846−0258 proposed above, we would not see the heated polar caps in quiescence. In addition, there is no significant change in flux or spectrum of the power-law component during the outburst. Also, magnetar pulse profiles are typically more complex than that of J1846−0258 (Hu et al. 2019), but this could result from less persistent magnetic field activity as well. In addition, the X-ray luminosity of J1846−0258 is less than its spin-down power, whereas for magnetars the X-ray luminosity exceeds the spin-down power by several orders of magnitude. Finally, one could argue that the SED of J1846−0258 is closer to the smooth SR-like spectrum of RPPs like the Crab and B1509−58 (Kuiper et al. 2018) that do not show the sharp cutoff predicted for magnetar SEDs (Wadiasingh et al. 2019). However, at the moment there are no detected spectral points in the SED of J1846−0258 between 200 keV and 30 MeV, so a sharp attenuation cutoff could exist. In addition, both the quiescent and outburst X-ray spectra of J1846−0258 are very close to the spectrum of magnetar RXS J1708−40 (Kuiper & Hermsen 2009). The true test then of a pulsar-like versus a magnetar-like model for PSR J1846−0258 is a measurement of its SED between 200 keV and 30 MeV.

Regardless of whether the pulsar-like or magnetar-like model for J1846−0258 is more plausible, the existence and behavior of J1846−0258 and J1119−6127 suggest a continuum of neutron stars that lie between RPPs and magnetars (Pons & Perna 2011; Perna & Pons 2011). The enhanced quiescent thermal emission observed from them and several other high-B RPPs supports such a continuum (Kaspi & McLaughlin 2005; Ng et al. 2012; Olausen et al. 2013; Hu et al. 2017). In fact, the characteristics of J1846−0258 are similar to those of transient anomalous X-ray pulsars (Livingstone et al. 2010) and may indicate a link between RPPs and magnetars. An additional similarity between RPPs and magnetars is the discovery of a wind nebula around the canonical magnetar Swift J1834.9−0846 (Younes et al. 2016). What is less clear is their direction of evolution. Espinoza et al. (2011, 2022) showed that the high-B pulsar J1734−333 is evolving toward the magnetars (based on its braking index). There is no evidence for magnetar X-ray behavior for this pulsar, but this result may indicate the direction of evolution. Since both J1846−0258 and J1119−6127 are very young, it is possible that a stronger interior magnetic field is in the process of emerging over a timescale $<10^3$–10^4 yr (Bhattacharya & Soni 2008). After the 2006 outburst of J1846−0258, its braking index was observed to decrease by 18% (Livingstone et al. 2011), which could be caused by an increase in magnetic field strength (Blandford et al. 1983; Ho 2015). Yet, such sources may have been born with stronger magnetic fields that are in the final stage of decaying (Pons et al. 2009; Viganò et al. 2013; Gourgouliatos et al. 2016). Continued X-ray monitoring of J1846−0258 as well as expanded spectral coverage will be crucial in understanding of its true nature and place in neutron star evolution.

Acknowledgments

This work was supported by the National Aeronautics and Space Administration (NASA) through the NICER mission, the Astrophysics Explorers Program, and through the NICER

Guest Investigator Program. This work partly made use of data supplied by the UK Swift Science Data Centre at the University of Leicester. This research has also made use of data obtained with NuSTAR, a project led by Caltech, funded by NASA and managed by NASA/JPL, and has utilized the NUSTARDAS software package, jointly developed by the ASDC (Italy) and Caltech (USA). C.-P.H. acknowledges support from the National Science and Technology Council in Taiwan through grant 109-2112-M-018-009-MY3 and 112-2112-M-018-004-MY3. W.C.G.H. acknowledges support through grants 80NSSC21K2035 and 80NSSC22K1308 from NASA. C.M. E. acknowledges support from the grant ANID FONDECYT 1211964.

Facilities: NICER, NuSTAR, *Swift*(XRT).

Software: HEASoft, XSPEC.

ORCID iDs

Chin-Ping Hu https://orcid.org/0000-0001-8551-2002
Lucien Kuiper https://orcid.org/0000-0002-7889-6586
Alice K. Harding https://orcid.org/0000-0001-6119-859X
George Younes https://orcid.org/0000-0002-7991-028X
Harsha Blumer https://orcid.org/0000-0003-4046-884X
Teruaki Enoto https://orcid.org/0000-0003-1244-3100
Keith Gendreau https://orcid.org/0000-0001-7115-2819

References

Archibald, R. F., Kaspi, V. M., Tendulkar, S. P., & Scholz, P. 2016, ApJL, 829, L21
Baring, M. G., & Harding, A. K. 2007, Ap&SS, 308, 109
Beloborodov, A. M. 2013, ApJ, 762, 13
Bhattacharya, D., & Soni, V. 2008, BASIP, 25, 47
Blandford, R. D., Applegate, J. H., & Hernquist, L. 1983, MNRAS, 204, 1025
Blumer, H., Safi-Harb, S., McLaughlin, M. A., & Fiore, W. 2021, ApJL, 911, L6
Burrows, D. N., Hill, J. E., Nousek, J. A., et al. 2005, SSRv, 120, 165
Espinoza, C. M., Lyne, A. G., Kramer, M., Manchester, R. N., & Kaspi, V. M. 2011, ApJL, 741, L13
Espinoza, C. M., Vidal-Navarro, M., Ho, W. C. G., Deller, A., & Chatterjee, S. 2022, A&A, 659, A41
Gavriil, F. P., Gonzalez, M. E., Gotthelf, E. V., et al. 2008, Sci, 319, 1802
Gehrels, N., Chincarini, G., Giommi, P., et al. 2004, ApJ, 611, 1005
Gotthelf, E. V., Vasisht, G., Boylan-Kolchin, M., & Torii, K. 2000, ApJL, 542, L37
Gourgouliatos, K. N., Wood, T. S., & Hollerbach, R. 2016, PNAS, 113, 3944
Harding, A. K., & Kalapotharakos, C. 2015, ApJ, 811, 63
Harding, A. K., & Kalapotharakos, C. 2017, in Proc. of the 7th Int. Fermi Symp. (Trieste: PoS), 6
Harding, A. K., Venter, C., & Kalapotharakos, C. 2021, ApJ, 923, 194
Helfand, D. J., Agüeros, M. A., & Gotthelf, E. V. 2003, ApJ, 592, 941
Ho, W. C. G. 2015, MNRAS, 452, 845
Hu, C.-P., Ng, C.-Y., & Ho, W. C. G. 2019, MNRAS, 485, 4274
Hu, C.-P., Ng, C. Y., Takata, J., Shannon, R. M., & Johnston, S. 2017, ApJ, 838, 156
Kalapotharakos, C., Brambilla, G., Timokhin, A., Harding, A. K., & Kazanas, D. 2018, ApJ, 857, 44
Kaspi, V. M., & Beloborodov, A. M. 2017, ARA&A, 55, 261
Kaspi, V. M., & McLaughlin, M. A. 2005, ApJL, 618, L41
Krimm, H. A., Lien, A. Y., Page, K. L., et al. 2020, GCN, 28187, 1
Kuiper, L., Harding, A. K., Enoto, T., et al. 2020, ATel, 13985, 1
Kuiper, L., & Hermsen, W. 2009, A&A, 501, 1031
Kuiper, L., & Hermsen, W. 2015, MNRAS, 449, 3827
Kuiper, L., Hermsen, W., & Dekker, A. 2018, MNRAS, 475, 1238
Kuiper, L., Hermsen, W., den Hartog, P. R., & Urama, J. O. 2012, ApJ, 748, 133
Kumar, H. S., & Safi-Harb, S. 2008, ApJL, 678, L43
Livingstone, M. A., Kaspi, V. M., & Gavriil, F. P. 2010, ApJ, 710, 1710
Livingstone, M. A., Ng, C. Y., Kaspi, V. M., Gavriil, F. P., & Gotthelf, E. V. 2011, ApJ, 730, 66
Ng, C. Y., Kaspi, V. M., Ho, W. C. G., et al. 2012, ApJ, 761, 65
Ng, C. Y., Slane, P. O., Gaensler, B. M., & Hughes, J. P. 2008, ApJ, 686, 508
Olausen, S. A., Zhu, W. W., Vogel, J. K., et al. 2013, ApJ, 764, 1
Perna, R., & Pons, J. A. 2011, ApJL, 727, L51
Pons, J. A., Miralles, J. A., & Geppert, U. 2009, A&A, 496, 207
Pons, J. A., & Perna, R. 2011, ApJ, 741, 123
Viganò, D., Rea, N., Pons, J. A., et al. 2013, MNRAS, 434, 123
Wadiasingh, Z., Younes, G., Baring, M. G., et al. 2019, BAAS, 51, 292
Wilms, J., Allen, A., & McCray, R. 2000, ApJ, 542, 914
Younes, G., Kouveliotou, C., Kargaltsev, O., et al. 2016, ApJ, 824, 138